

ROSAT SURVEY DIFFUSE X-RAY BACKGROUND MAPS. II.

S. L. SNOWDEN,^{1,2,3,4} R. EGGER,¹ M. J. FREYBERG,¹ D. MCCAMMON,⁴ P. P. PLUCINSKY,^{1,4,5}
W. T. SANDERS,⁴ J. H. M. M. SCHMITT,¹ J. TRÜMPER,¹ AND W. VOGES¹

Received 1996 September 20; accepted 1997 March 10

ABSTRACT

This paper presents new maps of the soft X-ray background from the *ROSAT* all-sky survey. These maps represent a significant improvement over the previous version in that (1) the position resolution of the PSPC has been used to improve the angular resolution from $\sim 2^\circ$ to $12'$, (2) there are six energy bands that divide each of the previous three into two parts, and (3) the contributions of point sources have been removed to a uniform source flux level over most of the sky. These new maps will be available in electronic format later in 1997.

In this paper we also consider the bright emission in the general direction of the Galactic center in the 0.5–2.0 keV band, and the apparent absorption trough that runs through it along the Galactic plane. We find that while the northern hemisphere data are confused by emission from Loop I, the emission seen south of the plane is consistent with a bulge of hot gas surrounding the Galactic center (in our simple model, a cylinder with an exponential fall-off of density with height above the plane). The cylinder has a radial extent of ~ 5.6 kpc. The X-ray emitting gas has a scale height of 1.9 kpc, an in-plane electron density of $\sim 0.0035 \text{ cm}^{-3}$, a temperature of $\sim 10^{6.6} \text{ K}$, a thermal pressure of $\sim 28,000 \text{ cm}^{-3} \text{ K}$, and a total luminosity of $\sim 2 \times 10^{39} \text{ ergs s}^{-1}$ using a collisional ionization equilibrium (CIE) plasma emission model.

Subject headings: diffuse radiation — Galaxy: center — surveys — X-rays: galaxies — X-rays: ISM

1. INTRODUCTION

Initial maps of the soft X-ray background (SXRB) in the 0.1–2.0 keV range derived from the *ROSAT* (*Röntgensatellit*; Trümper 1983, 1992) all-sky survey (Snowden & Schmitt 1990; Voges 1992) data were presented in Snowden et al. (1995b, hereafter Paper I). The Paper I maps are a significant improvement over previous surveys (McCammon et al. 1983; Marshall & Clark 1984; Garmire et al. 1992) in angular resolution and statistical significance but do not utilize fully the angular and spectral resolution capabilities of the Position Sensitive Proportional Counter (PSPC; Pfeffermann et al. 1987). They were created from an intermediate data-reduction product that binned the data from the entire $\sim 2^\circ$ field of view (i.e., treated the PSPC as a “light bucket”) into $40'$ pixels in three energy bands.

In this paper, we present maps that were produced using Rev0-processed survey data (Gruber 1992; Voges et al. 1992). Although the maps are binned in $12' \times 12'$ pixels to provide reasonable statistics, they use the full angular resolution of the X-ray Telescope (XRT; Aschenbach 1988) and PSPC (1.8 50% encircled energy radius averaged over the field of view) combination for event positioning and point-source removal. These new maps have been produced in six energy bands, with each of the three energy bands from Paper I effectively divided into two parts. (A final incremental improvement is planned for 1998. These future maps will be based on a reprocessing of the survey data and

will have better energy calibration, more sensitive point-source removal, improved noncosmic background subtraction. There will be additional pulse-height bands that will allow a full sampling of the PSPC energy resolution.)

In this paper we discuss the R2/R1 band ratio, or “color” of the $\frac{1}{4}$ keV radiation, and its implications for the location of the emitting material. Consistent with an earlier paper (Snowden, Schmitt, & Edwards 1990) based on the ratio of the Wisconsin survey (McCammon et al. 1983) C-band (0.16–0.284 keV) to B-band (0.13–0.188 keV) data, we find evidence for a large-scale variation in the hardness, with the Galactic center direction in general being harder and the Galactic anticenter direction softer.

We also consider the bright 0.5–2.0 keV enhancement in the general direction of the Galactic center. Some have argued that the enhancement is due to emission associated with Loop I (e.g., Hayakawa et al. 1977), others suggest that much of it originates as far away as the Galactic center (e.g., Garmire & Nugent 1981; Sofue 1994), while still others argue for the intermediate approach of some contribution from both sources (e.g., Egger 1994). We use the latitude dependence of the excess and the absorption trough in the Galactic plane to argue that the southern hemisphere part of the enhancement is almost entirely due to emission from a Galactic X-ray bulge, while the northern part is a superposition of bulge and Loop I emission.

2. DATA REDUCTION

2.1. X-Ray Data

The maps presented here are based on the same Standard Analysis Software System (SASS) reduction (Rev0) as the maps in Paper I but are substantially improved by additional processing, including finer pulse-height and angular binning. The data were collected during the *ROSAT* all-sky survey, which used the PSPC of the XRT. The details of the survey observation intervals, survey geometry, and most of

¹ Max-Planck-Institut für Extraterrestrische Physik, D-85740 Garching, Germany.

² Code 662, NASA/Goddard Space Flight Center, Greenbelt, MD 20771.

³ Universities Space Research Association.

⁴ Department of Physics, University of Wisconsin-Madison, 1150 University Avenue, Madison, WI 53706.

⁵ Harvard-Smithsonian Center for Astrophysics, 60 Garden Street, Cambridge, MA 02138.

the SASS processing used for this analysis can be found in Paper I.

In order to use the full angular resolution of the PSPC and to improve the spectral resolution used for the maps, the survey photon event files (OMAS) were used rather than the BFLGZ files (where the counts were summed in 10 s intervals) used for Paper I. These files contain among other entries, the time of detection, detector position, sky direction, and pulse-height invariant (PI) channel (the measure of the photon energy) of all accepted events. PI channel data have had their pulse heights corrected for temporal, electronic, and spatial gain variations. There are 90 such data sets, each consisting of photon event data from a $2^\circ \times 360^\circ$ strip on the sky. There are multiple files for sky regions (strips) covered by different survey intervals. Each strip is centered on a great circle that contains the ecliptic poles. They are spaced by 2° in ecliptic longitude, making them tangential to one another at the ecliptic plane. While there is significant overlap between the strips at higher ecliptic latitude, and particularly at the ecliptic poles where all strips contain data for the same region, by time selection each event appears in only one strip.

The sky-pixel size used during this data reduction is $1.6' \times 1.6'$. This size oversamples the survey-averaged point response of $\sim 1.8'$ (50% encircled energy radius) and loses no useful angular resolution. In addition, there are in general too few X-rays detected in a $1.6'$ pixel to make such fine pixels useful for analysis. Binning the data to achieve useful statistical significance typically requires sky pixels of several hundred square arcminutes, depending on the exposure and intrinsic brightness of the sky in a particular band. For bright objects such as the Cygnus Loop, finer binning may be advantageous. Each event was read from the photon event files and added to one of six $2^\circ \times 360^\circ$ maps with $1.6' \times 1.6'$ pixels according to its pulse height. The six energy bands are the same as those described in Snowden et al. (1994b), except that the R1 and not the R1L band is used here and the R3 band is not used. Table 1 lists the PI channel limits. Figure 1 shows the band response functions, i.e., the effective area of a band as a function of energy. Because of the limited energy resolution of the PSPC (it varies from $E/\Delta E \sim 1$ to $E/\Delta E \sim 3$ between $\frac{1}{4}$ keV and 1.5 keV), a limited number of broad bands effectively conveys the available spectral information.

2.2. Noncosmic Background Exclusion and Modeling

The same time selection described in Paper I was used in the creation of the high-resolution maps. Briefly, the

TABLE 1
BROAD ENERGY BAND DEFINITIONS

Band Name	PI Channels	Energy ^a (keV)
R1	8–19	0.11–0.284
R2	20–41	0.14–0.284
R4	52–69	0.44–1.01
R5	70–90	0.56–1.21
R6	91–131	0.73–1.56
R7	132–201	1.05–2.04

^a 10% of peak response. The R1 and R2 bands share the same upper energy limit because they are bounded by the carbon K α absorption edge of the PSPC entrance window.

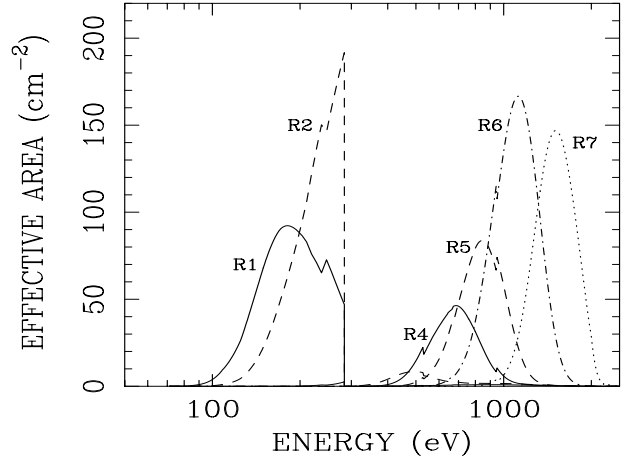


FIG. 1.—On-axis band response curves for the *ROSAT* bands of Table 1. The sharp break at 0.284 keV is due to the carbon K α absorption edge of the PSPC entrance window. The small unlabeled peak at ~ 500 eV is part of the R2 band response.

geometry of the sky survey afforded 15 or more independent observations of each sky element over a time of at least two days. This multiple coverage of each sky pixel was used to search for short period (several minutes to $\lesssim 4\text{--}5$ hr) background enhancements. The time intervals of enhancements above a 5σ threshold were then excluded from the processing. Time periods at which the particle background might be unpredictable were also excluded.

The modeling and subtraction of the remaining non-cosmic background components were also based on the methods and results of Paper I. However, while the light-bucket analysis of Paper I required only the modeling of background count rates, these high-resolution maps also required the modeling of the sky coordinates of the background counts. In essence, the modeled count rates from the long-term enhancements (LTEs, Snowden et al. 1994b), scattered solar X-rays (SB, Snowden & Freyberg 1993), and particle background (PB, Snowden et al. 1992; Plucinsky et al. 1993) were converted to modeled counts by multiplying the count rate by the exposure over short time steps. The modeled counts for each time step were then distributed over the detector field of view on the sky in the $2^\circ \times 360^\circ$ strips using normalized detector response (quantum efficiency) maps. These maps incorporate the telescope vignetting and any detector efficiency variations, including shadowing by the window support structure. The normalized detector response maps were scaled so that the sum of all map pixels equaled 1, thus the number of modeled background counts when multiplied by the detector map and transformed into sky coordinates gave the probability distribution for those modeled counts in sky pixels. This is very similar to the method described in Snowden et al. (1994b) for the reduction of *ROSAT* PSPC pointed-observation data, where the noncosmic background components are discussed in greater detail.

The selection on detector position suggested in Plucinsky et al. (1993) and Snowden et al. (1994b) was followed for this analysis. Regions near the edges of the detectors, where the anode wires are connected to the sides, are affected by higher particle background rates. The small fraction of these regions that lies within the open area of the window has been excluded.

TABLE 2
POINT-SOURCE EXCLUSION THRESHOLDS

Band	PI Channels	Threshold ^a (counts s ⁻¹)
R1 + R2 ($\frac{1}{4}$ keV or soft).....	8–41	0.025
R4 + R5 ($\frac{3}{4}$ keV)	52–90	0.020
R6 + R7 (1.5 keV)	91–201	0.020

^a Point-source count rates above which sky pixels affected by the source were masked out.

2.3. Exposure Correction and Effective Exposure

Exposure correction for these high-resolution SXRB maps required processing the data in much the same manner as was required to model the noncosmic background components. The main difference was in the normalization of the detector maps for the casting of the exposure into sky pixels. The detector maps were normalized so that the average on-axis value of the map was equal to 1.0. When the normalized detector map was multiplied by the deadtime-corrected exposure and cast into sky coordinates in the $2^\circ \times 360^\circ$ strips, the result was an effective exposure map corrected for vignetting, detector artifacts, obscuration by the window support structure, and any other efficiency variations. When the counts in the corresponding map pixel are divided by this exposure, the resulting count rate is normalized to the effective “on-axis” response of the XRT/PSPC.

The units of the soft X-ray background maps presented here are counts s⁻¹ arcmin⁻² (scaled by 10^6 when convenient; the field of view is $\sim 10^4$ arcmin²). As discussed in the previous paragraph, the maps are scaled to the surface brightness that would be observed if the optical axis were centered on a given sky pixel. Thus, when modeling these data, the on-axis values for the effective area (as a function of energy) should be used. It should be noted that although the effective exposure procedure described here corrects for the spatial variation of the response caused by the window support structure (and other detector efficiency variations), it does not include the average transmission of the window support mesh (78%) nor that of the detector window. For modeling these data (as well as for pointed observations), the average mesh transmission and window transmission should be included in the on-axis effective area function.

2.4. Point-Source Masking

In order to provide a statistically uniform point-source removal, we have chosen a flux threshold for which the existing survey source catalog is complete over 90% of the sky. Point-source masks in three bands (R1 + R2 band, R4 + R5 band, and R6 + R7 band) were created from the RASS-I survey source catalog using the thresholds that are listed in Table 2. The RASS-I catalog has 50,000 sources (detected in the broad band with hardness ratios), while the present RASS-II catalog (Voges et al. 1996) contains $\sim 80,000$ sources (detected in soft, hard, and broad bands). (Point-source masks derived from the RASS-II catalog will be incorporated into the next generation maps.) The fundamental sky-pixel size of $1.6' \times 1.6'$ allows some flexibility in the masking procedure; the number of $1.6' \times 1.6'$ pixels masked out for a specific source in the $2^\circ \times 360^\circ$ strips was dependent on the source count rate and source extent. The minimum source-excision radius was 3.5, or 2.2 of the $1.6'$ pixels.

3. MAPS

With the observed photon events, modeled background counts, exposure, and point-source masks produced for each $2^\circ \times 360^\circ$ strip, the task of creating the maps is straightforward. We have used six Zenith Equal Area projections (Greisen & Calabretta 1996) in Galactic coordinates to cover the sky. This projection provides a minimum of distortion of shapes near the boundaries while maintaining a constant pixel solid angle. The six centers (poles) for the projections are the north and south Galactic poles and at $0^\circ, 90^\circ, 180^\circ$, and 270° along the Galactic plane. There is an overlap between adjacent submaps as they cover a minimum diameter of $\sim 100^\circ$. The pixel size is $12' \times 12'$. As noted above, there are often too few counts in a single pixel of a single band to be statistically useful, but the small pixel size allows flexibility for binning into regions of arbitrary shape.

Figures 2, 3, and 4 (Plates 2, 3, and 4) show the data from the R1 + R2 (R12 or $\frac{1}{4}$ keV), R4 + R5 (R45 or $\frac{3}{4}$ keV), and R6 + R7 (R67 or 1.5 keV) bands, respectively, in the six projections. The data have been smoothed for this presentation using a 3×3 pixel sliding box. In late 1997 maps in these projections for all six individual energy bands will be available over the World Wide Web from the Max-Planck-Institut für extraterrestrische Physik (MPE; see http://rosat_svc.mpe-garching.mpg.de) or from a mirrored site at the Goddard Space Flight Center (GSFC; see <http://heasarc.gsfc.nasa.gov/docs/rosat/rosgef.html>). In addition, we have included maps of the *IRAS* 100 μm data (see Wheelock et al. 1994) in the same projections (Fig. 5 [Pl. 5]). The data shown here are from Schlegel, Finkbeiner, & Davis (1997) and have had their zero level and gain corrected using *DIRBE* data. The *IRAS* 100 μm data can be converted to hydrogen column densities in units of 10^{20} cm⁻² by multiplying by 1.44 (Schlegel, Finkbeiner, & Davis 1997). Figure 6 (Plate 6) shows the X-ray data, and Figure 11c below shows the *IRAS* data in all-sky Aitoff-Hammer projections.

The difference in structure between the $\frac{1}{4}$ keV and harder bands is pronounced and provides insights into the origin of the diffuse background components. Because the cross section for the absorption of X-rays by the ISM goes roughly as $E^{-8/3}$, by looking in a given direction at different energies it is possible to probe to different distances in the Galaxy. At $\frac{1}{4}$ keV, one optical depth is about 1×10^{20} H cm⁻², giving a mean free path of ~ 65 pc with the average Galactic disk space density of $n(\text{H}) \sim 0.5 \text{ cm}^{-3}$, ignoring molecular gas (e.g., Bloemen 1987). Thus, most of the R1 and R2 band emission in Galactic-plane projections must originate locally, particularly in the Galactic center direction where a thick wall of H I is reached at ~ 50 pc (Frisch & York 1983; Paresce 1984). On the other hand, for the 1.5 keV band (R6 + R7), one optical depth is $\sim 5 \times 10^{21}$ H cm⁻² (depending on the assumed spectrum), corresponding to a mean free path of ~ 3.2 kpc in the plane assuming the same average space density of $n(\text{H}) \sim 0.5 \text{ cm}^{-3}$. (This value is less appropriate in the Galactic plane where molecular gas can contribute significantly to absorption).

Figure 7 shows the count rates per unit emission measure for the six bands as a function of thermal emission temperature (Raymond & Smith 1977; Raymond 1992) and absorbing column density (Morrison & McCammon 1983). The emission-measure units are cm⁻⁶ pc. Figure 8 repeats this as a function of power-law photon index. For use with

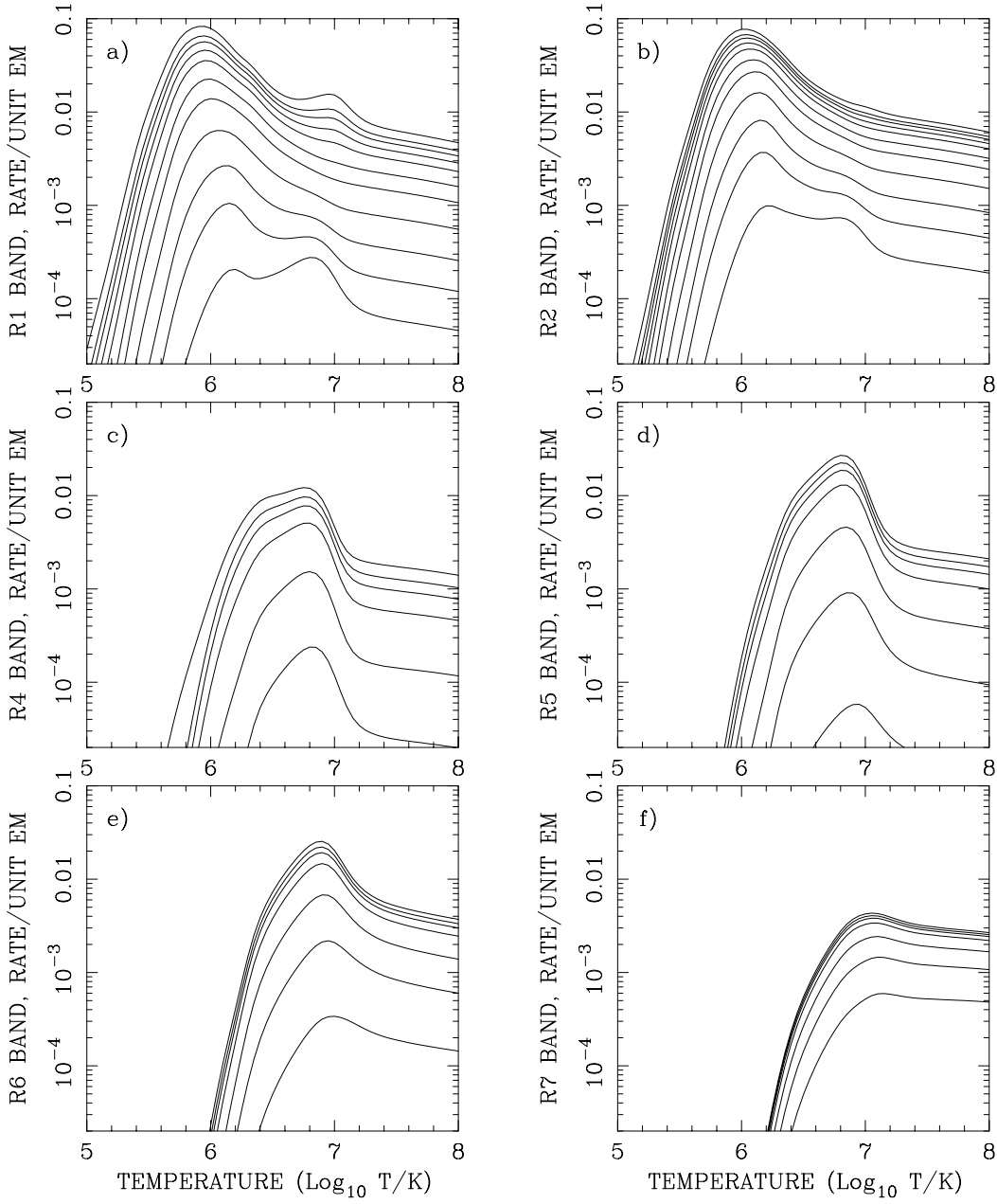


FIG. 7.—Model count rates per unit emission measure for thermal emission spectra in the six bands. The model rates are in units of counts s^{-1} arcmin $^{-2}$ and the emission measure is in units of cm^{-6} pc. The different curves, starting from the top, are for 0, 0.15, 0.25, 0.40, 0.60, 1.0, 1.5, 2.5, 4.0, 6.0, and 10.0×10^{20} H I cm^{-2} for the R1 and R2 bands (*a* and *b*) and 0, 5, 10, 20, 50, 100, and 200×10^{20} H I cm^{-2} for the R4 through R7 bands (*c*–*f*).

the maps presented here, Figure 9 (Freyberg 1994) repeats the model curves of Figures 7 and 8 for the combined R12, R45, and R67 bands. Figure 10 shows the R2/R1 band ratio as a function of thermal-emission temperature and absorbing column and the R67/R45 band ratio as a function of both thermal-emission temperature and power-law photon index, and absorbing column. The total sky fluxes shown on the maps are in most cases the sum of two or more components, each with its own source spectrum and absorbing column. For instance, at high Galactic latitude, the $\frac{1}{4}$ keV diffuse background is comprised of, at least, a local thermal component (unabsorbed), a Galactic halo thermal component (absorbed), and an extragalactic power-law component (absorbed). The 0.5–2.0 keV band is comprised of an extragalactic power law plus Galactic thermal emission intermixed with absorption.

4. THE $\frac{1}{4}$ keV BAND

The $\frac{1}{4}$ keV band is the R1 band plus the R2 band. As noted above, at this energy the bulk of the observed flux in the Galactic plane in all likelihood originates locally. At higher Galactic latitudes this is no longer the case as the Galactic column of H I drops to 1–3 optical depths, allowing the observation of emission in the Galactic halo and beyond. The existence of a variable Galactic halo at $\frac{1}{4}$ keV has been demonstrated by a number of *ROSAT* observations (e.g., Hasinger et al. 1993; Burrows & Mendenhall 1991; Snowden et al. 1991, 1994a; Herbstmeier et al. 1995; Wang & Yu 1995), and in addition there is an observable flux of extragalactic origin (e.g., Snowden & Pietsch 1995; Cui et al. 1996; Barber, Roberts, & Warwick 1996). While the quantitative mix of emission components has been diffi-

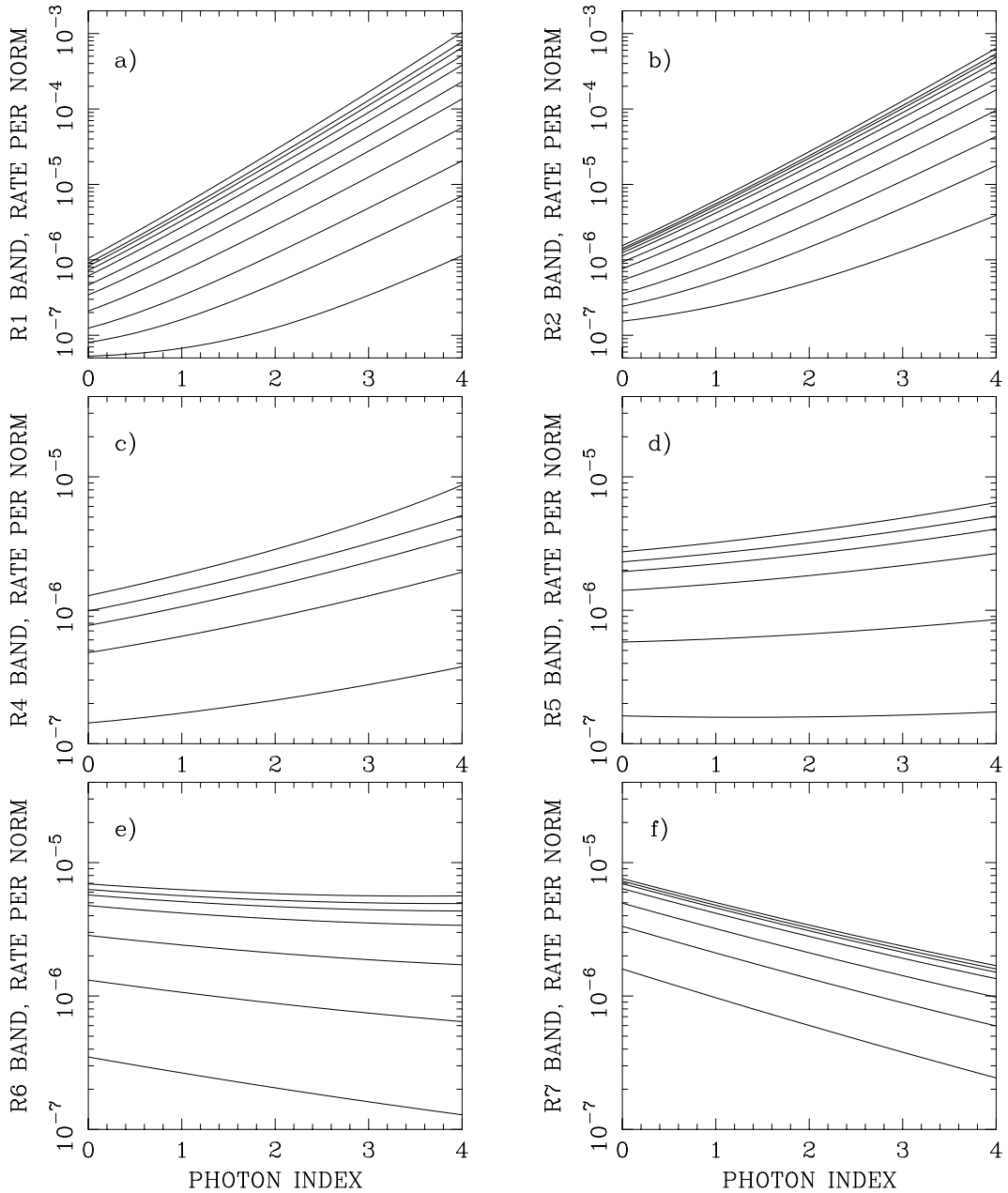


FIG. 8.—Model count rates for power-law photon spectra ($E^{-\alpha}$, where α is the power-law index and E is in keV) per unit normalization. The model rates are in units of counts s^{-1} arcmin $^{-2}$ and the normalization is in units of photons $cm^{-2} s^{-1} sr^{-1} keV^{-1}$. The different curves are for the same absorbing columns as in Fig. 7.

cult to disentangle (although see Snowden et al. 1997), some success has come from these shadowing experiments. By examining “shadows” of H I and molecular clouds, i.e., the negative correlation between cloud column density and $\frac{1}{4}$ keV surface brightness, it is possible to separate the observed flux into foreground and background components. With the knowledge of the distances to the clouds, determined by absorption-line or reddening studies of stars, we can begin to map out in three dimensions the distribution of hot plasma responsible for the observed X-ray flux.

The detailed negative correlation between the $\frac{1}{4}$ keV band (Fig. 2) and *IRAS* 100 μm (Fig. 5) intensities at high Galactic latitude is striking. The high angular resolution provided by the *ROSAT* all-sky survey allows the observation of detailed structure in the diffuse background on scales less than a degree (e.g., Snowden et al. 1994a;

Snowden et al. 1995a; Herbstmeier et al. 1995; Moritz et al. 1997). In regions of relatively low *IRAS* 100 μm intensity ($\lesssim 4$ MJy sr^{-1}), the negative correlation is very good. Since the absorption (shadowing) of emission originating behind the material shown in the 100 μm maps is the most reasonable explanation for such structures, and since by the intensity selection these regions are at high Galactic latitude, this implies an extensive distribution of X-ray emitting material located above most of the gas of the Galactic disk.

Before the observation of shadows of high- z clouds in the $\frac{1}{4}$ keV band (Burrows & Mendenhall 1991; Snowden et al. 1991), the displacement model (Sanders et al. 1977; Snowden et al. 1990) was the simplest explanation of the observed properties of emission in that band. The motivation for this model was the observation that the ratio of the C and B bands of the Wisconsin survey (0.16–0.284 keV and

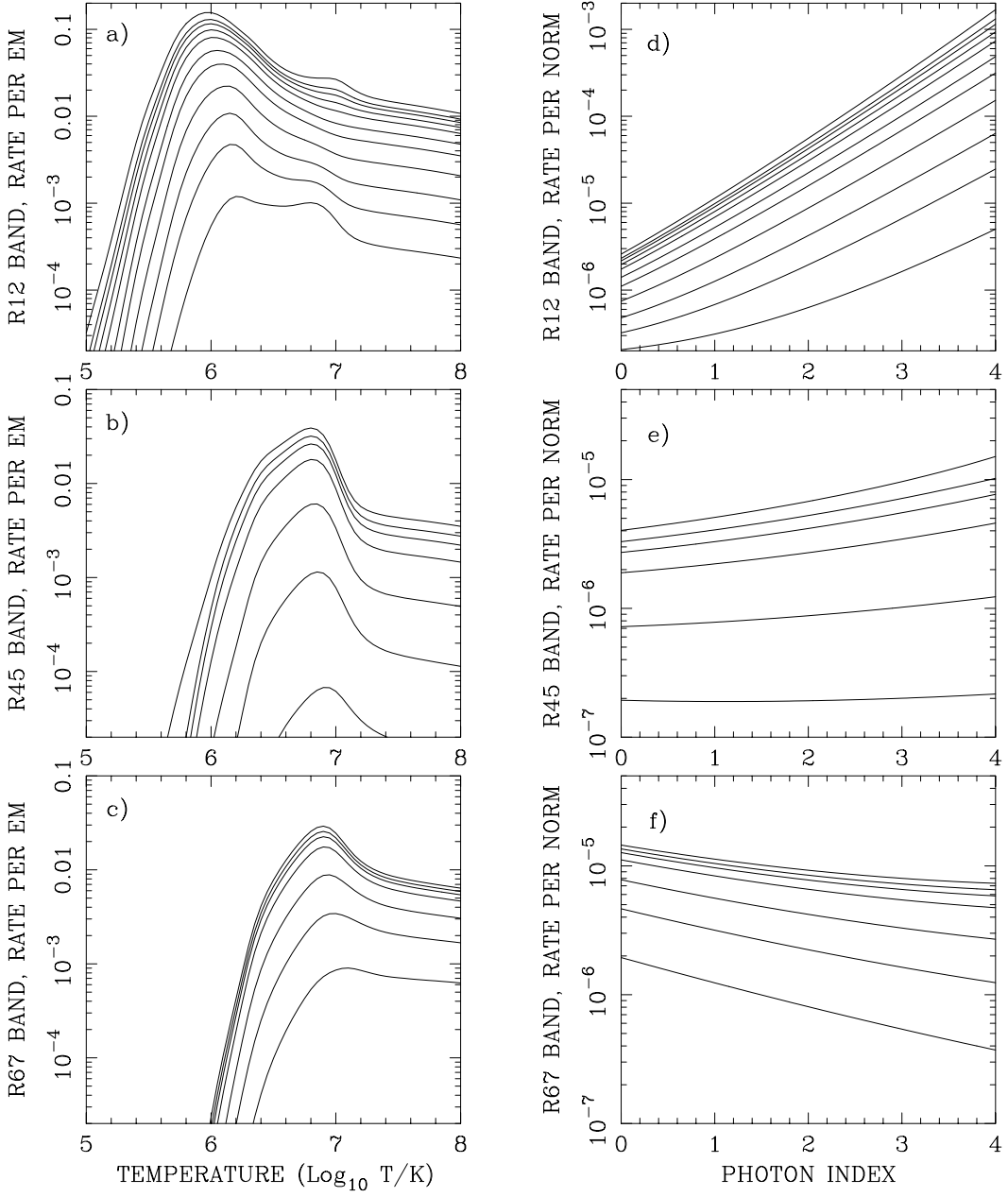


FIG. 9.—Model count rates per unit emission measure for thermal emission spectra in the (a) R12, (b) R45, and (c) R67 bands. The units and the N_{H} curves are the same as for Fig. 7. Model count rates for power-law photon spectra per unit normalization for the (d) R12, (e) R45, and (f) R67 bands. The units and the N_{H} curves are the same as for Fig. 8.

0.13–0.188 keV, respectively; McCammon et al. 1983) showed only $\pm 25\%$ variation across the sky (Snowden et al. 1990). Since absorption by as little as $1 \times 10^{20} \text{ H I cm}^{-2}$ of interstellar gas would change the C/B ratio by a factor of three, it is difficult to construct a reasonable model where there is any substantial variation in the interstellar absorption. In the displacement model, the bulk of the observed flux originates as thermal emission in a Local Hot Bubble (LHB, Cox & Reynolds 1987) that surrounds the Sun with an average radius of ~ 100 pc. In this simplistic model, the conditions were assumed to be uniform throughout the LHB leading to a prediction of a constant hardness of the observed spectrum.

We now consider this result with the *ROSAT* R1 and R2 band data. Figure 11a (Plate 7) displays an all-sky map of

the R2/R1 band ratio. The figure shows the same general features as the C/B ratio, but there is a wealth of additional detail visible due to the higher angular resolution and much greater number of counts. Some of the structures can be attributed to discrete Galactic features. The hard, high-latitude arc ($l, b \sim 290^\circ, 60^\circ$ to $0^\circ, 70^\circ$ to $20^\circ, 30^\circ$) is part of the North Polar Spur (NPS), the limb-brightened edge of a nearby superbubble (e.g., Iwan 1980; Egger 1995). The hard region at ($l, b \sim 320^\circ, 20^\circ$, diameter $D \sim 30^\circ$) could be due to emission from the same feature (perhaps with some Galactic bulge contribution) shining through a “hole” in the H I that separates the Sco-Cen (Loop I) bubble from the LHB. The hard, small circles at ($l, b \sim 260^\circ, -3^\circ, D \sim 10^\circ$) and ($l, b \sim 75^\circ, -7^\circ, D \sim 5^\circ$) are the Vela and Cygnus Loop supernova remnants (SNRs), respectively. The

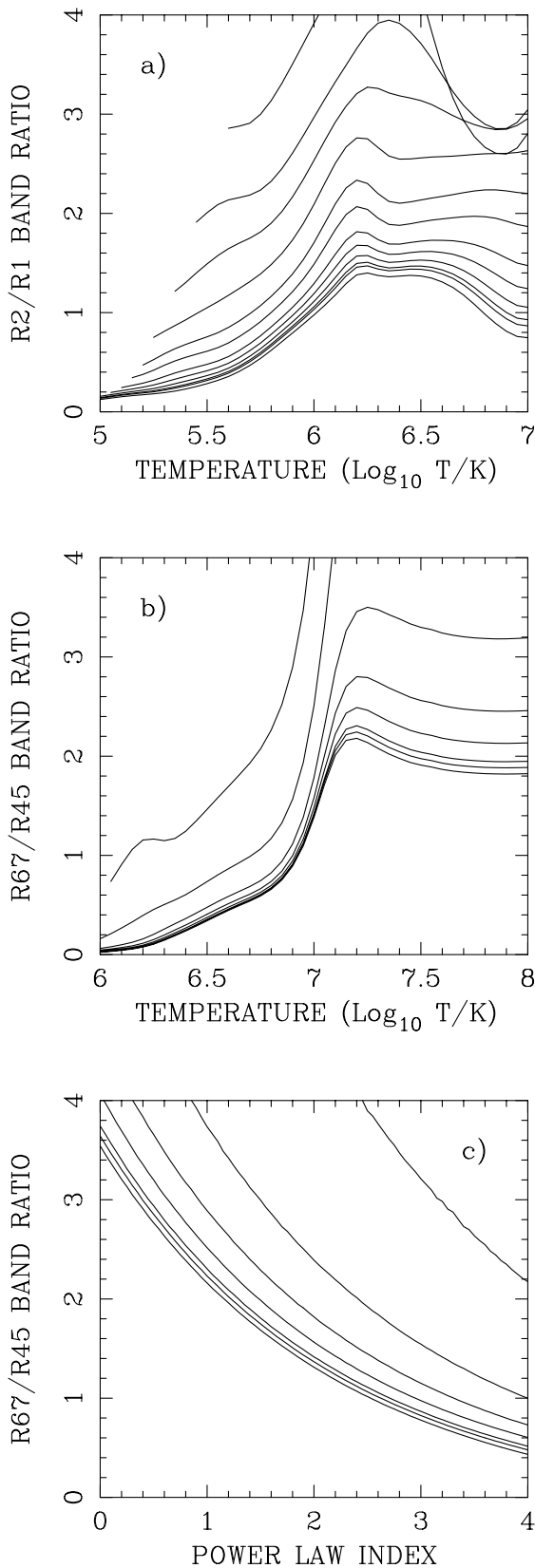


FIG. 10.—(a) Model ratios for the R2/R1 band ratio as a function of thermal emission temperature and absorbing column. Starting from the bottom, the curves are for 0, 0.10, 0.15, 0.25, 0.40, 0.60, 1.0, 1.5, 2.5, 4.0, 6.0, and $10.0 \times 10^{20} \text{ H cm}^{-2}$. (b) Model ratios for the 1.5 keV to $\frac{3}{4}$ keV band ratio as a function of thermal emission temperature and absorbing column. Starting from the bottom, the curves are for 0, 1, 2, 5, 10, 20, and $50 \times 10^{20} \text{ H cm}^{-2}$. (c) Same as (b) except for power-law photon spectra, $E^{-\alpha}$, where α is the power-law index and E is in keV.

Monoceros/Gemini enhancement centered at ($l, b \sim 205^\circ, 10^\circ, D \sim 25^\circ$) and the Eridanus enhancement at ($l, b \sim 235^\circ, -40^\circ, D \sim 20^\circ$) are also apparent in the map. These features are thought to be, respectively, an old, isolated SNR (e.g., Plucinsky et al. 1996 and references therein) and a reheated SNR or wind-blown bubble (e.g., Burrows et al. 1993; Snowden et al. 1995a; Guo & Burrows 1997, and references therein). Another “feature” in the data, the sharp hard/soft break in the second quadrant near $l \sim 120^\circ$ running roughly north-south ($-15^\circ \lesssim b \lesssim 25^\circ$), is attributed to a problem in the noncosmic background subtraction, which will be corrected in future versions of these maps.

Discrete features and data reduction problems aside, there is still considerable structure in the hardness ratio. The hardness enhancement at ($l, b \sim 75^\circ, 30^\circ, D \sim 40^\circ$) is of particular note. The location of the enhancement at the same Galactic longitude as the Cygnus Superbubble, and therefore possibly in the halo above it, suggests that there has been a blow out of hot gas. One attractive aspect of this argument is that the blow out could explain the strong diffuse emission enhancement in the Galactic halo that backlights the Draco region (e.g., Burrows & Mendenhall 1991; Snowden et al. 1991). This possibility is discussed in Snowden et al. (1997).

The most striking feature of the R2/R1 band ratio map (aside from the obviously “hard” enhancements associated with Loop I and the Galactic center, which presumably have higher emission temperatures) is the high R2/R1 ratio around the edges of the major high-latitude enhancements. This is particularly noticeable around the bright areas near ($l, b \sim 70^\circ, 45^\circ$), and on the north side of the large enhancement at ($300^\circ \lesssim l \lesssim 30^\circ, b \sim -55^\circ$). (Compare Fig. 11a with Fig. 6a.) The R2/R1 ratio at the peaks of these enhancements tends to revert to levels not much higher than those far from the enhancement.

This is qualitatively just the behavior one would expect from a two-component source (a foreground unabsorbed component and a distant component absorbed by the column density of Galactic H I), where the bright spots are produced by the distant component shining through local minima in the interstellar medium (ISM) and where both components have approximately the same intrinsic spectrum. When the ISM is very thick, only the local component is observed. As the ISM starts to become more transparent, the observed flux is increased by transmitted X-rays from the distant component that have been hardened by the interstellar absorption, and therefore increase the net R2/R1 ratio. When the absorption becomes small, the total flux is maximized, but there is no longer any hardening of the distant component, so the R2/R1 ratio returns to its original value. Since the shadowing measurements of high- z clouds discussed at the beginning of this section show that much of the observed flux on these high-latitude enhancements originates far above the Galactic plane, it is tempting to assume that the enhancements are halo emission seen through low column density areas in the H I disk.

The problem with this attractive interpretation, however, is that the minimum Galactic H I column densities in the directions of the $\frac{1}{4}$ keV maxima are still $\sim 1-2$ optical depths, so the hardness should continue to increase toward the minimum H I direction. For it to go down again, one has to assume that the background component is intrinsically much softer than the foreground, about half the tem-

perature. The low emission efficiency and interstellar gas transmission then require extremely large emission measures assuming a collisional ionization equilibrium (CIE) plasma spectrum. Enhancements with higher column densities need even lower background temperatures. The difficulty is exacerbated by observations made in the 0.07–0.111 keV Be band, where the bright areas are just as enhanced as they are in the R12 band, but where the total H I absorption is more than 10 optical depths (Bloch et al. 1986; Juda et al. 1991). A more detailed analysis of the R2/R1 ratios offers some insights and is presented in Snowden et al. (1997).

5. THE 0.5–2.0 keV BAND

The flux observed in the *ROSAT* hard band is a mixture of Galactic and extragalactic emission. While progress is being made resolving the extragalactic component into discrete sources (e.g., Hasinger et al. 1993), the origin of the Galactic component is not well understood (see McCammon & Sanders 1990). At high latitudes in regions away from obvious Galactic emission enhancements (e.g., the Loop I/NPS complex in the Galactic center hemisphere), most of the flux is extragalactic in origin with $\gtrsim 60\%$ in the 1–2 keV band and $\sim 40\%$ in the 0.5–1.0 keV band resolved by deep-survey observations into discrete, mostly extragalactic, sources (Hasinger et al. 1993, 1996). In the Galactic plane, particularly in the Galactic center direction, the structure is very complicated with contributions from Galactic objects as near as 100 pc (Sco-Cen bubble) and possibly as far away as the Galactic bulge.

In the anticenter hemisphere there are considerably fewer discrete features. The lack of a deep intensity minimum along the plane, which should be caused by the absorption of the extragalactic flux, implies that there is Galactic emission distributed in such a manner to compensate for much of that absorption. However, the maps do show structure consistent with absorption (Freyberg et al. 1997) by the relatively nearby Taurus-Auriga molecular cloud complex and associated H I enhancement south of the Galactic anticenter (the $\sim \frac{1}{4}$ sr around $l, b \sim 180^\circ, -15^\circ$, Hobbs et al. 1988).

5.1. The Galactic Center Direction, Galactic Bulge or Loop I

The Galactic center direction at energies above 0.5 keV is about 6 times brighter than the typical high-latitude flux and shows considerable structure. Against this bright enhancement, some of the first images from the all-sky survey showed clear shadows cast by objects such as the Ophiuchus dark clouds ($l, b \sim 355^\circ, 17^\circ, D \sim 10^\circ$), and the images generally looked similar to large solid-angle optical images of this part of the Milky Way. There is also a deep intensity minimum or “absorption trough” along the plane in the Galactic center direction, from longitudes $\sim 315^\circ$ to $\sim 45^\circ$, which is seen most clearly at $\frac{3}{4}$ keV.

The origin of the bright enhancement is uncertain. Two possibilities, not mutually exclusive, are most likely. While the emission could originate in a Galactic center X-ray bulge, this is also the direction of the closest SNR/stellar wind bubble: the Sco-Cen Bubble or Radio Loop I. This bubble is centered at a distance of ~ 170 pc and has a radius of ~ 150 pc (e.g., de Geus, de Zeeuw, & Lub 1989; de Geus 1992; Egger 1995), therefore covering a large solid angle on the sky. First identified in the radio (e.g., Berkhuijsen, Haslam, & Salter 1971), its extent is clearly outlined in the northern hemisphere in continuum emission as an incomplete small circle on the sky (centered at $l, b \sim 329^\circ, 17.5^\circ$,

with a radius of $\sim 58^\circ$). From the results of Centurion & Vladilo (1991), in the direction of the center of Loop I the wall of the LHB is at a distance of more than 15 pc, while the near-side wall of the Sco-Cen Bubble is at a distance of $\lesssim 65$ pc. These distances provide an upper limit to the extent (thickness) of the separating wall, not a measurement of it. The morphology of Loop I in radio continuum emission is more confused near the Galactic plane, and there is no clear extension to the south (Berkhuijsen, Haslam, & Salter 1971), although Columb, Poppel, & Heiles (1980) found evidence for an expanding ring of H I consistent with such an extension down to $b \sim -30^\circ$. In both radio continuum and X-rays, the northeastern rim is clearly outlined by the extensive feature known as the NPS. Although fainter, the emission can be traced through the northern extent of the Loop and down toward lower Galactic latitude at $l \sim 270^\circ$.

There is considerable X-ray emission both north and south of the Galactic plane at lower latitudes in a region consistent with the interior of a small circle on the sky defined by extrapolating the northern hemisphere extent of Loop I. However, this emission is also roughly centered on the Galactic center ($l \sim 355^\circ$) as would be consistent with Galactic bulge emission. Placement of the low-latitude emission at either the Galactic center or in Loop I obviously has drastically different consequences for its interpretation.

To help resolve this question, data were summed from a 10° wide swath in the $\frac{3}{4}$ keV and 1.5 keV bands extending in latitude over $-85^\circ \lesssim b \lesssim 85^\circ$ near the Galactic center (centered on $l = 353^\circ$). The data are shown in Figure 12. The enhancement and the trough in the Galactic plane are clearly seen in both bands. The latitude profile of the surface

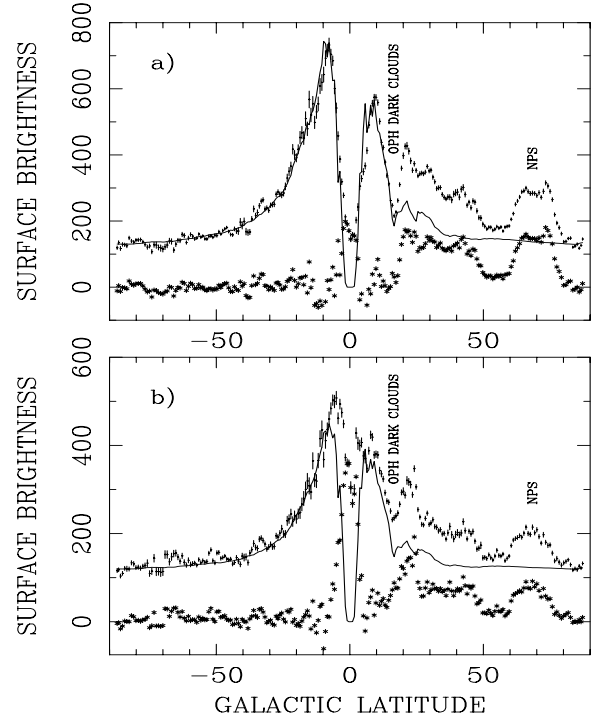


FIG. 12.—Cuts across the Galactic plane at $l = 353^\circ \pm 5^\circ$ in the (a) $\frac{3}{4}$ keV and (b) 1.5 keV bands. The upper points (with error bars) are the data, the curve is the prediction of the simple model described in the text, and the lower points are the residuals of the data minus the model. Surface brightness is in units of 10^{-6} counts s^{-1} $arcmin^{-2}$. Emission from Loop I including the NPS is not modeled.

brightness is considerably smoother in the southern hemisphere. In the north there are both emission (e.g., the NPS) and absorption (e.g., the Ophiuchus dark clouds) features. In the south, the excess emission extends at least to $b \sim -60^\circ$.

Figure 12a can be used to get an estimate for the optical depth in the absorption trough that lies in the Galactic plane, which can then be used to derive a rough estimate to the lower limit of absorbing material in front of the emission responsible for the $\frac{3}{4}$ keV enhancement. The trough count rate is $\sim 150 \times 10^{-6}$ counts s^{-1} arcmin $^{-2}$, while interpolating the high-latitude data in the absence of absorption would give a peak value of $\sim 900 \times 10^{-6}$ counts s^{-1} arcmin $^{-2}$ at $b = 0^\circ$. The ratio of 1:6 implies an optical depth of ~ 1.8 , and a foreground absorbing column of $4.4 \times 10^{21} \text{ H I cm}^{-2}$. If the observed enhancement originates from the Sco-Cen Bubble, there must be a thick band of absorbing material that is tightly confined to the Galactic plane lying $\sim 40 \pm 25$ pc from the Sun (Centurion & Vladilo 1991). This is the region between the Local Hot Bubble and Sco-Cen Bubble, assuming that Sco-Cen is roughly spherical and filled with hot gas. From Figure 3c, it can be seen that this material must extend for over 60° in longitude and no more than 10° in latitude. In addition, this required absorption component must explicitly "know" about the Galactic plane (i.e., lie within $\pm \sim 5$ pc of the Galactic plane as observed from Earth), which is unlikely in a local context. This does not prove that the enhancement *must* be distant, but we will proceed under the assumption that the bulk of the Galactic center enhancement (all of it for $b < -10^\circ$) arises from a Galactic bulge. We will show that this assumption is plausible and consistent with other observations.

5.2. A Galactic X-Ray Bulge

With the above assumption, what can be learned about the Galactic X-ray bulge? In order to model the latitude profile, we use a simple model with a cylindrical bulge of radius 5.6 kpc (assuming a solar circle of 8 kpc and a visible extent of the X-ray bulge of 90° in longitude from, e.g., Fig. 3c) with an exponential fall-off in density with height above the plane. The line-of-sight emission measure through the cylinder was integrated as a function of Galactic latitude. Foreground absorption was derived from a Galactic H I column density map (Dickey & Lockman 1990) with additional absorption derived from a CO Galactic plane map (Dame et al. 1987). The assumption that the entire column density is in front of the emission is likely to be reasonable for $|b| \gtrsim 15^\circ$ but will clearly fail near the Galactic plane.

The curves plotted in Figure 12 show the results of the modeling the southern hemisphere data. The northern-hemisphere curves use the emission parameters (temperature, plane density, and scale height) determined from the southern data. While the model curves in the northern hemisphere deviate strongly from the data, note that the data *always* lie above the model curves. This is consistent with the deviations being due to an *additional* emission component that can easily be explained by assigning some of the observed flux to Loop I structures (e.g., the NPS). Additional structure in the north is produced by the Ophiuchus dark clouds, which cause a deep absorption dip in the latitude profile.

The southern profile is well fitted for latitudes $b \lesssim -10^\circ$. Using thermal equilibrium spectral models (Raymond &

Smith 1977; Raymond 1992), one can derive a temperature of $10^{6.6}$ K, a base electron density of 0.0035 cm^{-3} (providing an in-plane thermal pressure of $\sim 28,000 \text{ cm}^{-3}$ K), and a scale height of 1.9 kpc (14°). Assuming that the distribution can be extrapolated to the Galactic plane and that it is symmetric with respect to the Galactic plane, integrating the space density distribution produces a total mass of $\sim 3.3 \times 10^7 M_\odot$. We stress again that we have made only plausibility arguments. The extent and form of the bulge are likely to be different from our assumed cylinder and the densities and pressures will be affected by the filling factor of the gas and the degree of ionization. The continuation of the bulge gas down to the plane requires an intermixing with the observed neutral and molecular material. However, with a scale height of ~ 1.9 kpc, the Galactic disk contains only a small part of the distribution.

Further support for a Galactic center/bulge origin for the 0.5–2.0 keV band enhancement comes from a recent paper (Park et al. 1997), where a deep shadow has been found to be cast by a giant molecular cloud (GMC) complex at ($l, b \sim 10^\circ, 0^\circ$) at a distance 2–4 kpc. About 50% of the observed 0.5–2.0 keV band intensity in that direction originates beyond the complex. The estimated unabsorbed intensities are 1700×10^{-6} counts s^{-1} arcmin $^{-2}$ for the $\frac{3}{4}$ keV band and 900×10^{-6} counts s^{-1} arcmin $^{-2}$ for the 1.5 keV band (this, however, does not include absorption by molecular gas, which could significantly increase the intensities). The intensity ratio implies a temperature of $10^{6.7}$ K. Given the uncertainty in "deabsorbing" the distant intensity, this is a perhaps remarkable agreement with the extrapolation of our model to the plane; 3900×10^{-6} counts s^{-1} arcmin $^{-2}$ for the $\frac{3}{4}$ keV band and 1700×10^{-6} counts s^{-1} arcmin $^{-2}$ for the 1.5 keV band (only a factor of 2 different) and a temperature of $10^{6.6}$ K.

Integrating the emission measure perpendicular to the Galactic disk produces a value for the face-on surface brightness of 980×10^{-6} counts s^{-1} arcmin $^{-2}$ in the 0.5–2.0 keV band. This increases to 1870×10^{-6} counts s^{-1} arcmin $^{-2}$ over the total ROSAT band, or 1.4×10^{-14} ergs s^{-1} cm $^{-2}$ arcmin $^{-2}$. Integrating over the entire bulge produces a luminosity of 1.9×10^{39} ergs s^{-1} . For the nearby face-on galaxy M101, Snowden & Pietsch (1995) find a temperature of $10^{6.53}$ K and a luminosity of 3.6×10^{39} ergs s^{-1} for the unresolved 0.5–2.0 keV emission. The 5.6 kpc radius is 50% of the Galaxy's D_{25} radius (the radius at which $V = 25$ mag arcsec $^{-2}$; de Vaucouleurs & Pence 1983), which is consistent with the extent of the emission region of M101 (60%) and other galaxies showing X-ray halos (e.g., Pietsch et al. 1994).

5.3. The 1.5 keV to $\frac{3}{4}$ keV Band Ratio

The variation over the sky of the 1.5 keV to $\frac{3}{4}$ keV band ratio, shown in Figure 11b, provides strong support for the existence of an extensive distribution of Galactic emission in the Galactic center hemisphere. Besides the effect of a number of discrete Galactic features (e.g., NPS, Vela and Cygnus SNRs, Cygnus Superbubble, and the bright Galactic center enhancements), Figure 11b shows a large-scale variation over the sky. A striking feature in the image is the hard stripe along the Galactic plane, which flares out to higher latitudes near the anticenter. Comparison with the $\frac{3}{4}$ keV, 1.5 keV, and IRAS 100 μm maps strongly implies that this is an absorption effect. Along the plane both the $\frac{3}{4}$ keV and 1.5 keV bands exhibit troughs, but the $\frac{3}{4}$ keV trough is

deeper presumably because it reaches higher optical depths in the disk after shorter path lengths. Note, however, that both bands are nonzero along the Galactic plane even though the Galactic disk is optically thin. This requires a diffuse Galactic component that is not entirely understood. The hardness extension to higher latitudes in the anticenter direction correlates with the apparent shadowing by the Taurus-Auriga molecular cloud complex and associated H I enhancement discussed above.

Away from the plane the Galactic center hemisphere, even excluding the region and extrapolation of Loop I, is significantly softer than the anticenter hemisphere. Since this effect is seen at higher Galactic latitudes in regions of low column density (i.e., low optical depth), it is unlikely to be due to absorption. It is therefore an indication of a large-scale variation in Galactic emission, specifically an enhancement in the Galactic center hemisphere. The region of required additional emission extends well beyond Loop I and is therefore unlikely to be associated with it, although Loop I strongly contributes to the softness in the Galactic center region.

We note that while the R2/R1 band ratio map (Fig. 11a) shows a hardening of the background from the Galactic anticenter to center, the R67/R45 band ratio map (Fig. 11b) shows a hardening in the opposite direction. This is consistent with the fact that the likely additional emission from the putative X-ray bulge is softer than the extragalactic emission, which is significant in the 0.5–2.0 keV band, and harder than the emission from the Local Hot Bubble that dominates the $\frac{1}{4}$ keV band data.

6. CONCLUSION

We have presented improved maps of the soft X-ray diffuse background in the 0.1–2.0 keV band from the

ROSAT all-sky survey. The new versions have much better angular resolution, and point sources have been removed to a uniform flux level. The maps will be available in digital format in 1997 through the Max-Planck-Institut für extraterrestrische Physik *ROSAT* Guest Observer Facility. Access details will be placed on the World Wide Web through MPE and GSFC *ROSAT* home pages (see above).

We have also presented a preliminary analysis of the 0.5–2.0 keV band enhancement toward the Galactic center. While the results are not conclusive, we find it plausible that while Loop I provides significant emission in the northern hemisphere, the Galactic center enhancement is probably dominated by emission from a Galactic X-ray bulge. Parameters for the bulge emission are similar to those observed in other spiral galaxies, with an in-plane density of $\sim 0.0035 \text{ cm}^{-3}$, a scale height of $\sim 2 \text{ kpc}$, and a temperature of $\sim 10^{6.6} \text{ K}$, implying a thermal pressure in the plane of $P/k \sim 28,000 \text{ cm}^{-3} \text{ K}$. The total luminosity is $\sim 2 \times 10^{39} \text{ ergs s}^{-1}$.

The *ROSAT* project was supported by the Bundesministerium für Bildung, Wissenschaft, Forschung, und Technologie (BMBF/DARA) and the Max-Planck-Gesellschaft (MPG). These maps could, of course, never have been produced without the work of a large number of people at MPE who built and operated the XRT/PSPC and those who produced the SASS software. We would also like to thank our colleagues at MPE, Wisconsin, and GSFC for many long and fruitful discussions about both the data reduction for the all-sky survey and the interpretation of the results. This research was supported in part by DARA and the Max-Planck-Institut für extraterrestrische Physik, USRA, and by NASA under grants NAG 5-629, NAG 5-1438, NAG 5-1817, and NAG 5-1894.

REFERENCES

- Aschenbach, B. 1988, *Appl. Opt.*, 27, No. 8, 1404
- Barber, C. O., Roberts, T. P., & Warwick, R. 1996, *MNRAS*, 282, 157
- Berkhuijsen, E. M., Haslam, C. G. T., & Salter, C. T. 1971, *A&A*, 14, 252
- Bloch, J. J., Jahoda, K., Juda, M., McCammon, D., Sanders, W. T., & Snowden, S. L. 1986, *ApJ*, 308, L59
- Bloemen, J. B. G. M. 1987, *ApJ*, 322, 694
- Burrows, D. N., & Mendenhall, J. A. 1991, *Nature*, 351, 629
- Burrows, D. N., Singh, K. P., Good, J., Nousek, J. A., & Garmire, G. P. 1993, *ApJ*, 406, 97
- Centurion, M., & Vladilo, G. 1991, *ApJ*, 372, 494
- Columb, F. R., Poppel, W. G. L., & Heiles, C. 1980, *A&AS*, 40, 47
- Cox, D. P., & Reynolds, R. J. 1987, *ARA&A*, 25, 303
- Cui, W., McCammon, D., Sanders, W. T., Snowden, S. L., & Womble, D. S. 1996, *ApJ*, 468, 117
- Dame, T. M., et al. 1987, *ApJ*, 322, 706
- de Geus, E. J. 1992, *A&A*, 262, 258
- de Geus, E. J., de Zeeuw, P. T., & Lub, J. 1989, *A&A*, 216, 44
- de Vaucouleurs, G., & Pence, W. D. 1983, *AJ*, 83, 1163
- Dickey, J. M., & Lockman, F. J. 1990, *ARA&A*, 28, 215
- Egger, R. 1994, Ph.D. thesis, Technische Univ. München
- . 1995, *PASP*, 80, 45
- Freyberg, M. J. 1994, Ph.D. thesis, Technische Univ. München
- Freyberg, M. J. et al. 1997, in preparation
- Frisch, P. C., & York, D. G. 1983, *ApJ*, 271, L59
- Garmire, G. P., et al. 1992, *ApJ*, 399, 694
- Garmire, G. P., & Nugent, J. J. 1981, *BAAS*, 13, 786
- Greisen, E. W., & Calabretta, M. 1996, preprint
- Gruber, R. 1992, in *Data Analysis in Astronomy IV*, ed. V. Di Gesù et al. (New York: Plenum), 153
- Guo, Z., & Burrows, D. N. 1997, *ApJ*, 480, L51
- Hasinger, G., Burg, R., Giacconi, R., Hartner, G., Schmidt, M., Trümper, J., & Zamorani, G. 1993, *A&A*, 275, 1
- Hasinger, G., et al. 1996, in MPE Report 263, *Röntgenstrahlung from the Universe*, ed. H. U. Zimmermann, J. E. Trümper, & H. Yorke (Garching: MPE), 291
- Hayakawa, S., Kato, T., Nagase, F., Yamashita, K., Murakami, T., & Tanaka, Y. 1977, *ApJ*, 213, L109
- Herbstmeier, U., Mebold, U., Snowden, S. L., Hartmann, D., Burton, W. B., Moritz, P., Kalberla, P. M. W., & Egger, R. 1995, *A&A*, 298, 606
- Hobbs, L. M., Penprase, B. E., Welty, D. E., Blitz, L., & Magnani, L. 1988, *ApJ*, 327, 356
- Iwan, D. A. 1980, *ApJ*, 239, 316
- Juda, M., Bloch, J. J., Edwards, B. C., McCammon, D., Sanders, W. T., Snowden, S. L., & Zhang, J. 1991, *ApJ*, 367, 182
- Marshall, F. J., & Clark, G. W. 1984, *ApJ*, 287, 633
- McCammon, D., Burrows, D. N., Sanders, W. T., & Kraushaar, W. L. 1983, *ApJ*, 269, 107
- McCammon, D., & Sanders, W. T. 1990, *ARA&A*, 28, 657
- Moritz, P., Wennmacher, A., Herbstmeier, U., Mebold, U., Egger, R., & Snowden, S. L. 1997, *A&A*, submitted
- Morrison, R., & McCammon, D. 1983, *ApJ*, 270, 119
- Nousek, J. A., Fried, P. M., Sanders, W. T., & Kraushaar, W. L. 1982, *ApJ*, 258, 83
- Paresce, F. 1984, *AJ*, 89, 1022
- Park, S., Finley, J. P., Snowden, S. L., & Dame, T. M. 1997, *ApJ*, 476, L77
- Pfeffermann, E., et al. 1987, *Proc. SPIE*, 733, 519
- Pietsch, W., Vogler, A., Kahabka, P., Jain, A., & Klein, U. 1994, *A&A*, 284, 386
- Plucinsky, P. P., Snowden, S. L., Aschenbach, B., Egger, R., Edgar, R. J., & McCammon, D. 1996, *ApJ*, 463, 224
- Plucinsky, P. P., Snowden, S. L., Briel, U. G., Hasinger, G., & Pfeffermann, E. 1993, *ApJ*, 418, 519
- Raymond, J. C. 1992, *ApJ*, 384, 502
- Raymond, J. C., & Smith, B. W. 1977, *ApJS*, 35, 419
- Sanders, W. T., Kraushaar, W. L., Nousek, J. A., & Fried, P. M. 1977, *ApJ*, 217, L87
- Schlegel, D. J., Finkbeiner, D. P., & Davis, M. 1997, in preparation
- Snowden, S. L., Aschenbach, B., Pfeffermann, E., Burrows, D. N., & Sanders, W. T. 1995a, *ApJ*, 439, 399
- Snowden, S. L., Cox, D. P., McCammon, D., & Sanders, W. T. 1990, *ApJ*, 354, 211
- Snowden, S. L., Egger, R., Finkbeiner, D., Freyberg, M. J., & Plucinsky, P. P. 1997, *ApJ*, submitted
- Snowden, S. L., & Freyberg, M. J. 1993, *ApJ*, 404, 403

- Snowden, S. L., et al. 1995b, ApJ, 454, 643 (Paper I)
Snowden, S. L., Hasinger, G., Jahoda, K., Lockman, F. J., McCammon, D., & Sanders, W. T. 1994a, 430, 601
Snowden, S. L., McCammon, D., Burrows, D. N., & Mendenhall, J. A. 1994b, ApJ, 424, 714
Snowden, S. L., Mebold, U., Hirth, W., Herbstmeier, U., & Schmitt, J. H. M. M. 1991, Science, 252, 1529
Snowden, S. L., & Pietsch, W. 1995, ApJ, 452, 627
Snowden, S. L., Plucinsky, P. P., Briel, U., Hasinger, G., & Pfeffermann, E. 1992, ApJ, 393, 81
Snowden, S. L., & Schmitt, J. H. M. M. 1990, Ap&SS, 171, 207
Snowden, S. L., Schmitt, J. H. M. M., & Edwards, B. E. 1990, ApJ, 364, 118
Sofue, Y. 1994, ApJ, 431, L91
Trümper, J. 1983, Adv. Space Res., 2(4), 241
- Trümper, J. 1992, QJRAS, 33, 165
Voges, W. 1992, in Proc. Satellite Symp. 3, Space Science with Particular Emphasis on High-energy Astrophysics, ed. T. D. Guyenne & J. J. Hunt (Noordwijk: ESA), 9
Voges, W., et al. 1996, in MPE Report 263, Röntgenstrahlung from the Universe, ed. H. U. Zimmermann, J. E. Trümper, & H. Yorke (Garching: MPE), 637
Voges, W., et al. 1992, in Proc. Satellite Symp. 3, Space Science with Particular Emphasis on High-energy Astrophysics, ed. T. D. Guyenne & J. J. Hunt (Noordwijk: ESA), 223
Wang, Q. D., & Yu, K. C. 1995, AJ, 109, 698
Wheelock, S. L., et al. 1994, *IRAS* Sky Survey Atlas Explanatory Supplement (JPL Publication 94-11)

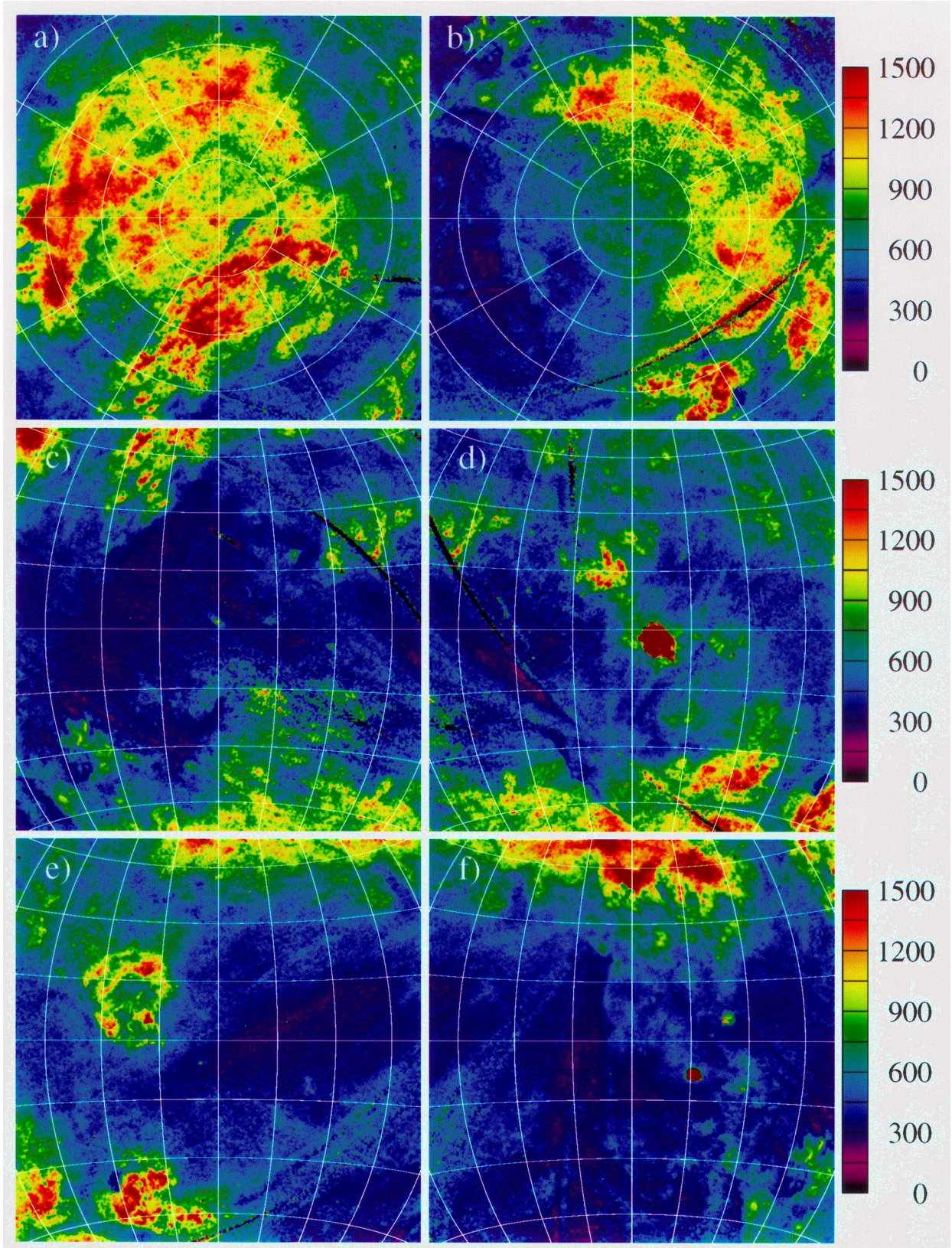


FIG. 2.—Maps of the $\frac{1}{4}$ keV (R12) band sky in the six projections: (a) north Galactic pole with $l = 0^\circ$ down and longitude increasing clockwise; (b) south Galactic pole with $l = 0^\circ$ up and longitude increasing counterclockwise; (c–f) the $l = 0^\circ$, $l = 270^\circ$, $l = 180^\circ$, and $l = 90^\circ$ centered Galactic plane projections, respectively. Lines of latitude are always spaced by 15° , while lines of longitude are spaced by 15° for the Galactic plane projections (longitude always increases to the left) and 30° in the polar projections. The units on the color bars are 10^{-6} counts s^{-1} $arcmin^{-2}$. Regions of missing data are black.

SNOWDEN et al. (see 485, 127)

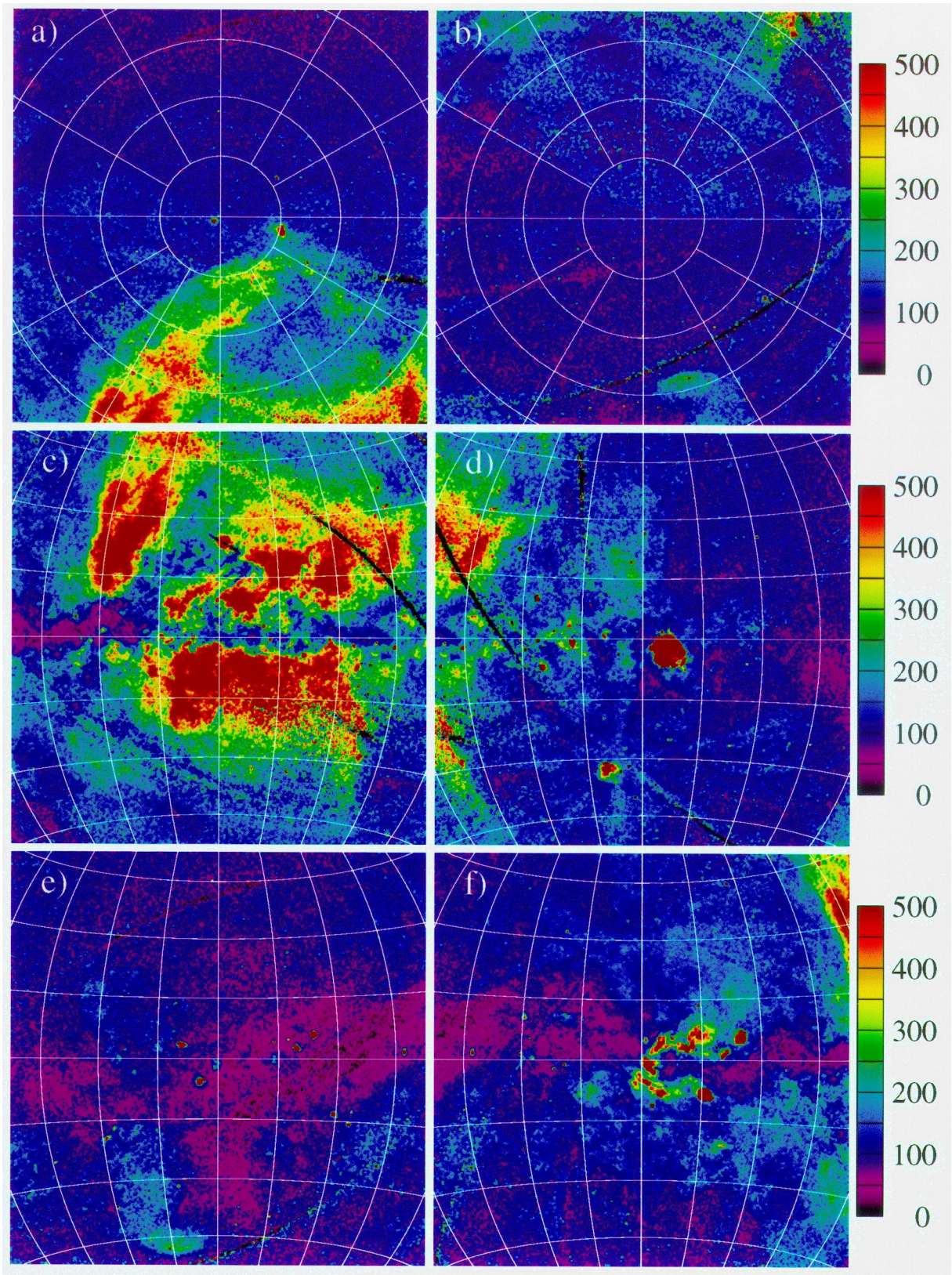


FIG. 3.—Same as Fig. 2 except for the $\frac{3}{4}$ keV (R45) band

SNOWDEN et al. (see 485, 127)

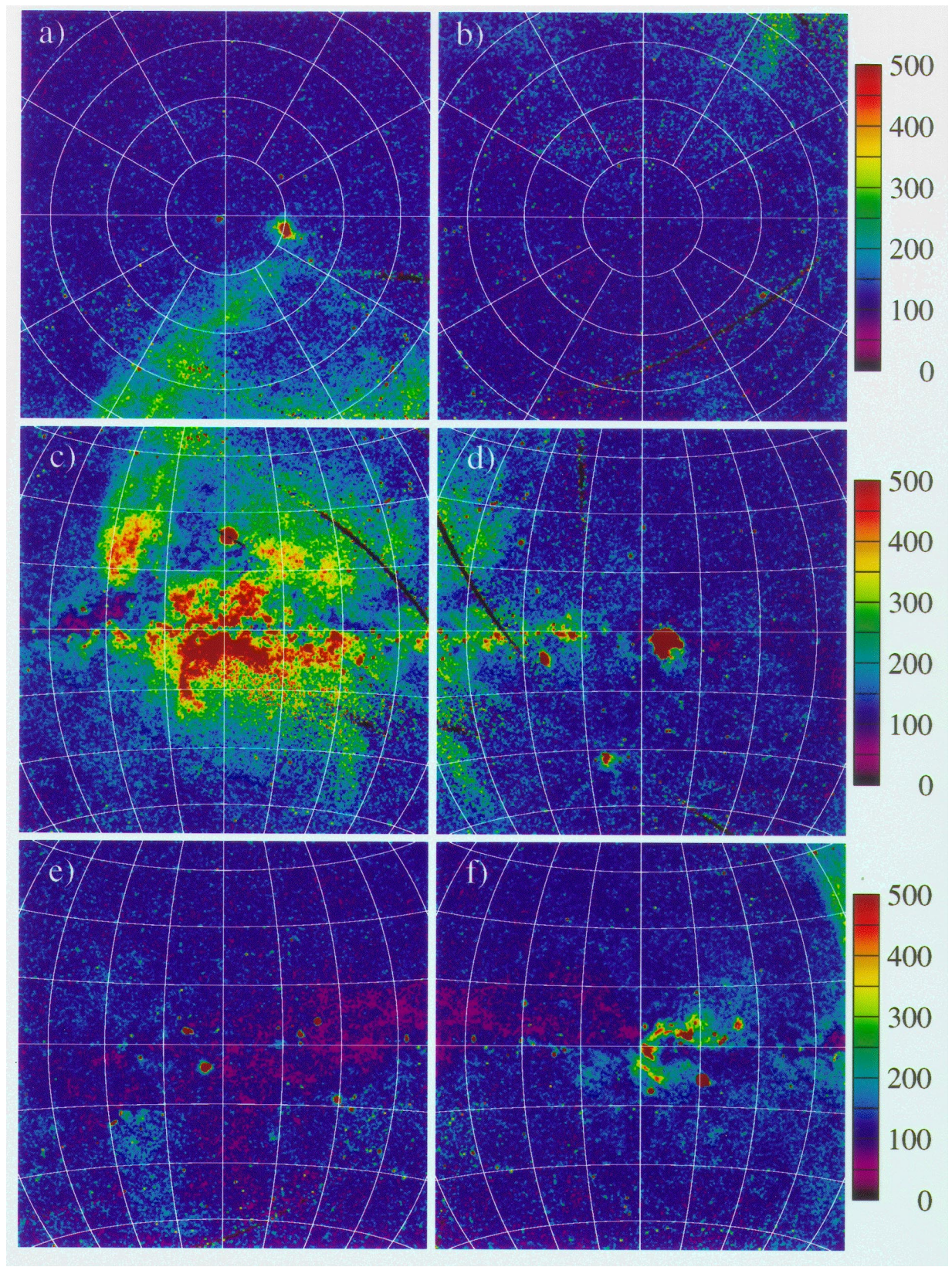


FIG. 4.—Same as Fig. 2 except for the 1.5 keV (R67) band

SNOWDEN et al. (see 485, 127)

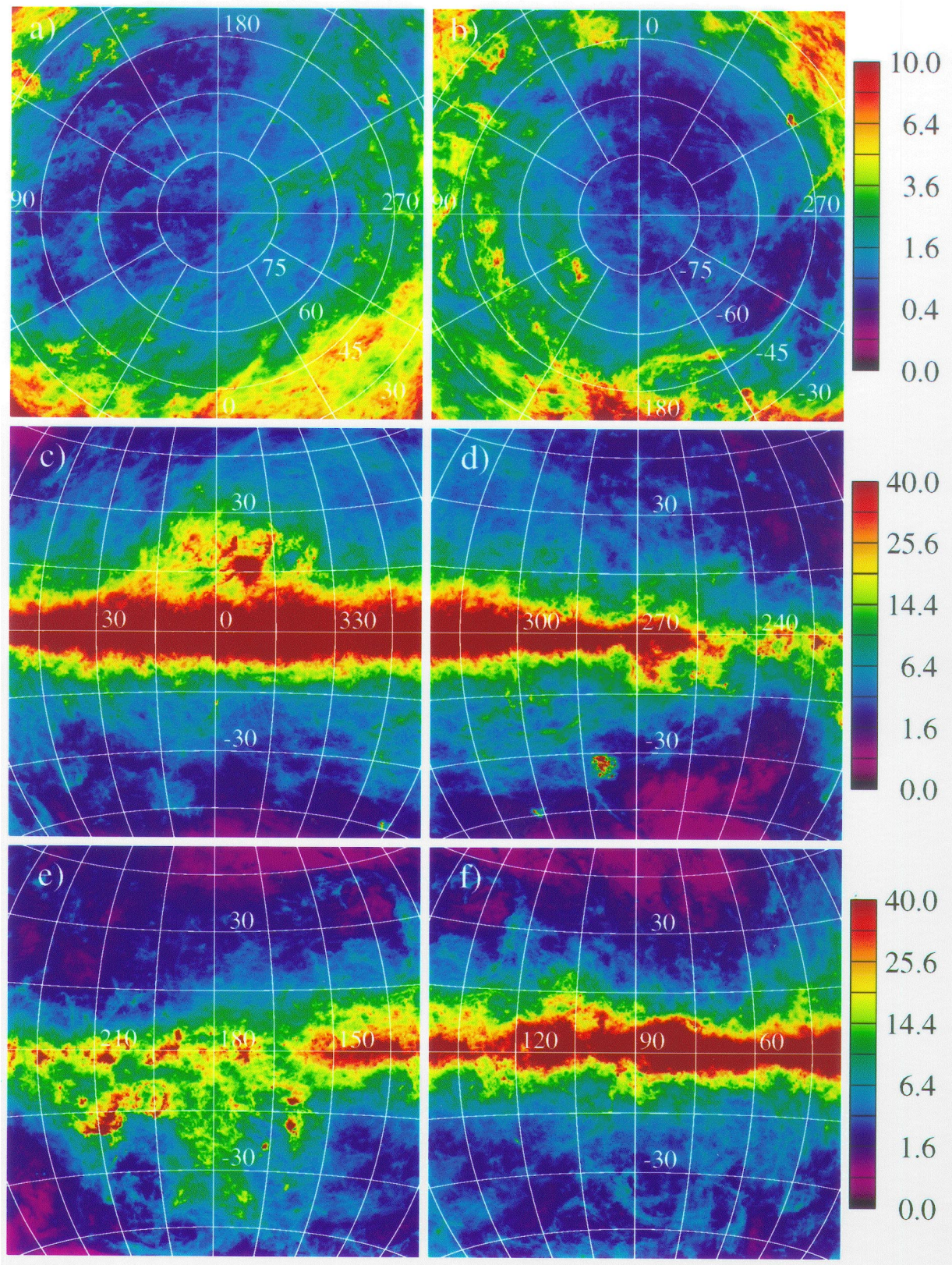


FIG. 5.—Same as Fig. 2 except for the *DIRBE*-corrected *IRAS* 100 μm data. The units on the color bars are MJy sr^{-1} .

SNOWDEN et al. (see 485, 127)

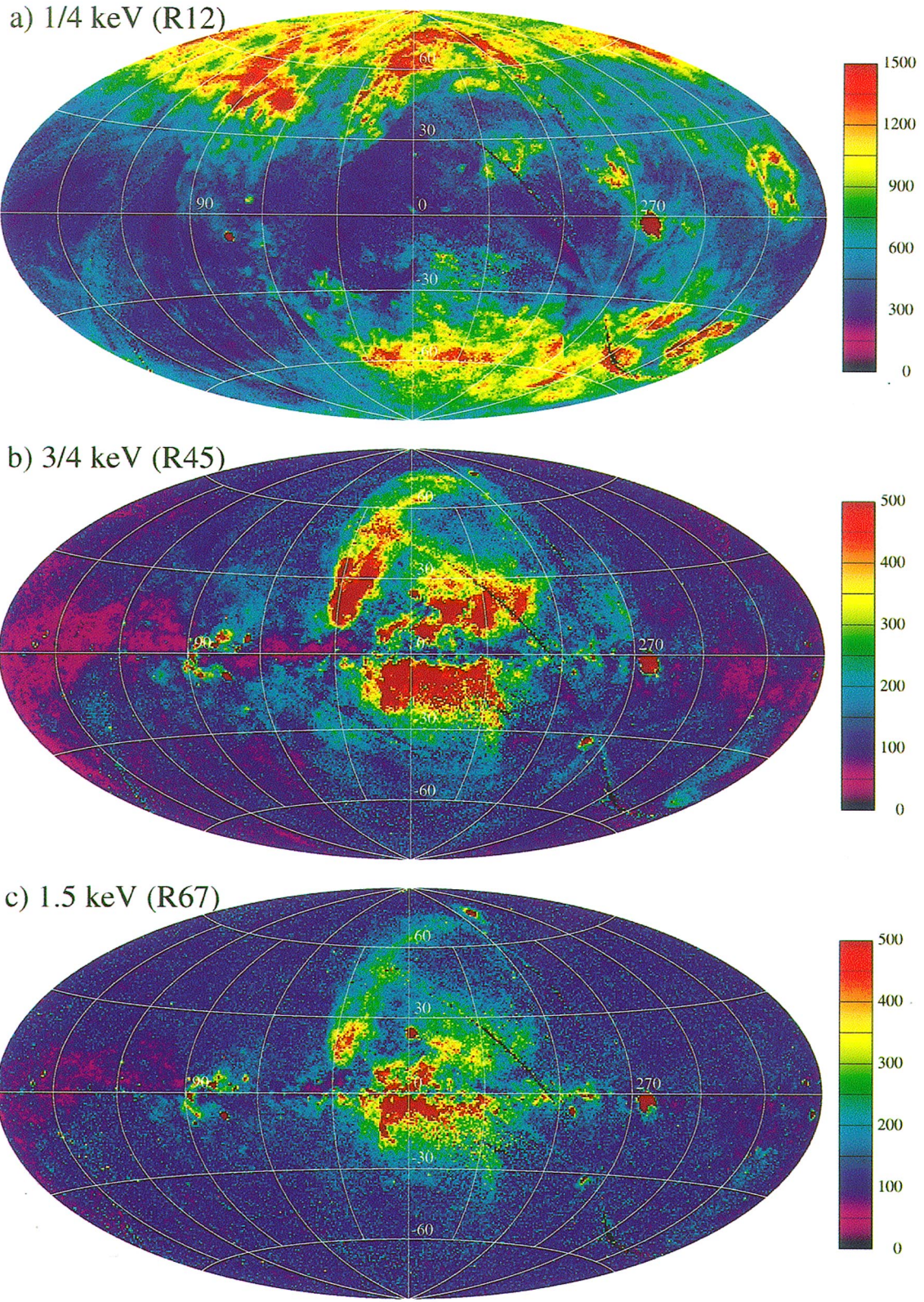


FIG. 6.—Aitoff-Hammer maps of the (a) R12, (b) R45, and (c) R67 band data. The projection is an Aitoff-Hammer equal area centered on the Galactic center with Galactic longitude increasing to the left. The values next to the color bars indicate the intensity and the units are 10^{-6} counts s^{-1} $arcmin^{-2}$. Regions of missing data are black.

SNOWDEN et al. (see 485, 127)

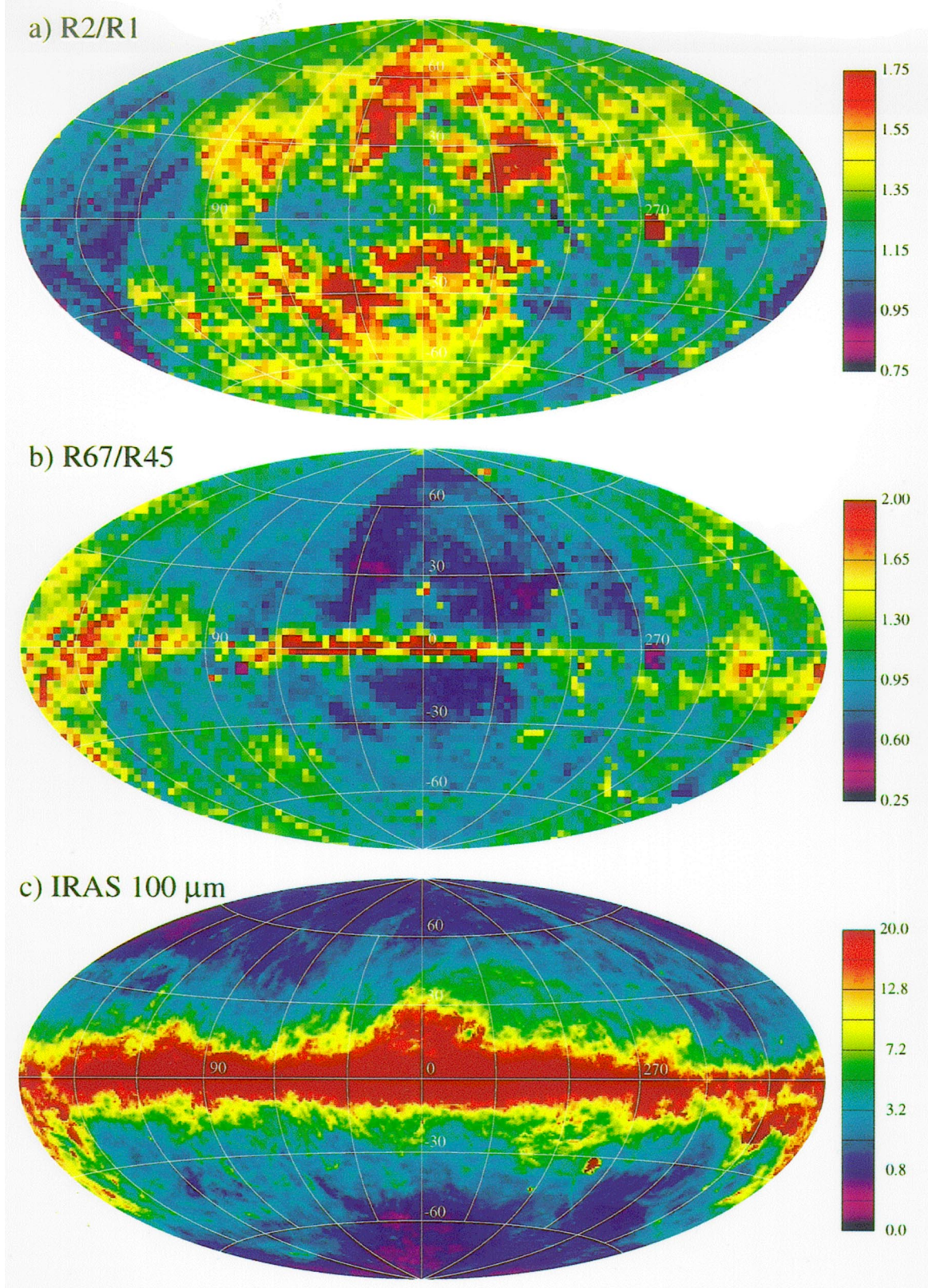


FIG. 11.—All-sky maps of (a) the R2/R1 band ratio, (b) the 1.5 keV to $\frac{3}{4}$ keV band ratio, and (c) the *IRAS* 100 μ m data. The projection, same as in Fig. 6, is an Aitoff-Hammer equal area centered on the Galactic center with Galactic longitude increasing to the left. The values next to the color bars indicate the ratio (a, b) or the intensity (c) in units of MJy sr⁻¹.

SNOWDEN et al. (see 485, 130)